Fast computational optimization of TMS coil placement for individualized electric field targeting

Supplemental Material

Luis J. Gomez[a,*], Moritz Dannhauer[a], Angel V. Peterchev[a,b,c,d,#]
[a] Department of Psychiatry and Behavioral Sciences, Duke University, NC 27710, USA
[b] Department of Electrical and Computer Engineering, Duke University, NC 27708, USA
[c] Department of Neurosurgery, Duke University, NC 27710, USA
[d] Department of Biomedical Engineering, Duke University, NC 27708, USA

Emails: ljgomez@purdue.edu, moritz.dannhauer@duke.edu, and angel.peterchev@duke.edu

[*]Present address: Department of Electrical and Computer Engineering, Purdue University, West Lafayette, IN 47907, USA

[#]Corresponding Author: Angel V. Peterchev
Address: 40 Duke Medicine Circle, Box 3620 DUMC, Durham, NC 27710, USA
Email: angel.peterchev@duke.edu
Phone: 919-684-0383

Derivation of reciprocity principle

Here we follow the derivation of reciprocity given in (Balanis, 1999), others can be found in introductory level electromagnetics texts (Harrington, 2001; Kong, 1986). Furthermore, we assume that the E-fields and sources are time-harmonic (i.e. $p(t) = exp(-j\omega t),$ where j is the imaginary unit and ω is the frequency). These equations will remain valid for general pulses via its application to the Fourier decomposition of the pulse (Plonsey, 1972).

Electromagnetic reciprocity is an equivalence relationship between two scenarios. In one scenario, impressed electric and magnetic currents $\mathbf{J_{TMS}}(\mathbf{r};t) = exp(-j\omega t)\mathbf{J_{TMS}}(\mathbf{r})$ and $\mathbf{K_{TMS}}(\mathbf{r};t) = exp(-j\omega t)\mathbf{K_{TMS}}(\mathbf{r})$ generate an E-field $\mathbf{E_{TMS}}(\mathbf{r};t) = exp(-j\omega t)\mathbf{E_{TMS}}(\mathbf{r})$ and H-field $\mathbf{H_{TMS}}(\mathbf{r};t) = exp(-j\omega t)\mathbf{H_{TMS}}(\mathbf{r})$. In the second scenario, electric and magnetic current sources $\mathbf{J_C}(\mathbf{r};t) = exp(-j\omega t)\mathbf{J_C}(\mathbf{r})$ and $\mathbf{K_C}(\mathbf{r};t) = exp(-j\omega t)\mathbf{K_C}(\mathbf{r})$ induces an E-field $\mathbf{E_C}(\mathbf{r};t) = exp(-j\omega t)\mathbf{E_C}(\mathbf{r})$ and H-field $\mathbf{H_C}(\mathbf{r};t) = exp(-j\omega t)\mathbf{H_C}(\mathbf{r})$. Faraday's and Ampere's law dictate the following for each scenario:

$$\nabla \times \mathbf{E_{TMS}}(\mathbf{r};t) = -\mathbf{K_{TMS}}(\mathbf{r};t) - j\omega\mu(\mathbf{r})\mathbf{H_{TMS}}(\mathbf{r};t), \tag{S1}$$

$$\nabla \times \mathbf{H_{TMS}}(\mathbf{r};t) = \mathbf{J_{TMS}}(\mathbf{r};t) + \sigma(\mathbf{r})\mathbf{E_{TMS}}(\mathbf{r};t) + j\omega\epsilon(\mathbf{r})\mathbf{E_{TMS}}(\mathbf{r};t), \tag{S2}$$

$$\nabla \times \mathbf{E_C}(\mathbf{r};t) = -\mathbf{K_C}(\mathbf{r};t) - j\omega\mu(\mathbf{r})\mathbf{H_C}(\mathbf{r};t), \tag{S3}$$

and

$$\nabla \times \mathbf{H_C}(\mathbf{r};t) = \mathbf{J_C}(\mathbf{r};t) + \sigma(\mathbf{r})\mathbf{E_C}(\mathbf{r};t) + j\omega\epsilon(\mathbf{r})\mathbf{E_C}(\mathbf{r};t). \tag{S4}$$

Here μ is the permeability, σ the conductivity of the medium. Equation (S1) dotted by $\mathbf{H_C}(\mathbf{r};t)$ subtracted from Eq. (S4) dotted by $\mathbf{E}(\mathbf{r};t)$ is

$$\mathbf{H_C}(\mathbf{r};t)\cdot\nabla\times\mathbf{E_{TMS}}(\mathbf{r};t) - \mathbf{E_{TMS}}(\mathbf{r};t)\cdot\nabla\times\mathbf{H_C}(\mathbf{r};t) = \nabla\cdot\left(\mathbf{E_{TMS}}(\mathbf{r};t)\times\mathbf{H_C}(\mathbf{r};t)\right) = -\mathbf{H_C}(\mathbf{r};t)\cdot\mathbf{K_{TMS}}(\mathbf{r};t) - j\omega\mathbf{H_C}(\mathbf{r};t)\cdot\mu(\mathbf{r})\mathbf{H_{TMS}}(\mathbf{r};t) - \mathbf{E_{TMS}}(\mathbf{r};t)\cdot\mathbf{J_C}(\mathbf{r};t) - \mathbf{E_{TMS}}(\mathbf{r};t)\cdot\sigma(\mathbf{r})\mathbf{E_C}(\mathbf{r};t) - j\omega\mathbf{E_{TMS}}(\mathbf{r};t)\cdot\epsilon(\mathbf{r})\mathbf{E_C}(\mathbf{r};t). \tag{S5}$$

Note that the first equality follows from the vector identity $\nabla\cdot(\mathbf{A}\times\mathbf{B}) = \mathbf{B}\cdot\nabla\times\mathbf{A} - \mathbf{A}\cdot\nabla\times\mathbf{B}$. Similarly, Eq. (S3) dotted by $\mathbf{H_{TMS}}(\mathbf{r};t)$ subtracted from Eq. (S2) dotted by $\mathbf{E_C}(\mathbf{r};t)$ is

$$\nabla\cdot\left(\mathbf{E_C}(\mathbf{r};t)\times\mathbf{H_{TMS}}(\mathbf{r};t)\right)=-\mathbf{H_{TMS}}(\mathbf{r};t)\cdot\mathbf{K_C}(\mathbf{r};t)-$$
$$j\omega\mathbf{H_{TMS}}(\mathbf{r};t)\cdot\mu(\mathbf{r})\mathbf{H_C}(\mathbf{r};t)-\mathbf{E_C}(\mathbf{r};t)\cdot\mathbf{J_{TMS}}(\mathbf{r};t)-\mathbf{E_C}(\mathbf{r};t)\cdot\sigma(\mathbf{r})\mathbf{E_{TMS}}(\mathbf{r};t)-j\omega\mathbf{E_C}(\mathbf{r};t)\cdot\epsilon(\mathbf{r})\mathbf{E_{TMS}}(\mathbf{r};t).\quad(\mathrm{S6})$$

Subtracting Eq. (S5) from Eq. (S6) results in the following

$$\nabla\cdot\left(\mathbf{E_C}(\mathbf{r};t)\times\mathbf{H_{TMS}}(\mathbf{r};t)-\mathbf{E_{TMS}}(\mathbf{r};t)\times\mathbf{H_C}(\mathbf{r};t)\right)=$$
$$\mathbf{H_C}(\mathbf{r};t)\cdot\mathbf{K_{TMS}}(\mathbf{r};t)-\mathbf{H_{TMS}}(\mathbf{r};t)\cdot\mathbf{K_C}(\mathbf{r};t)+\mathbf{E_{TMS}}(\mathbf{r};t)\cdot\mathbf{J_C}(\mathbf{r};t)-\mathbf{E_C}(\mathbf{r};t)\cdot\mathbf{J_{TMS}}(\mathbf{r};t).\qquad(\mathrm{S7})$$

Integrating over a volume $\mathbf{V}$ with boundary surface $\partial\mathbf{V}$ and applying gauss's law results in the following

$$\int_{\partial\mathbf{V}}\left(\mathbf{E_C}(\mathbf{r};t)\times\mathbf{H_{TMS}}(\mathbf{r};t)-\mathbf{E_{TMS}}(\mathbf{r};t)\times\mathbf{H_C}(\mathbf{r};t)\right)\cdot d\mathbf{r}=$$
$$\int_{\mathbf{V}}\mathbf{H_C}(\mathbf{r};t)\cdot\mathbf{K_{TMS}}(\mathbf{r};t)-\mathbf{H_{TMS}}(\mathbf{r};t)\cdot\mathbf{K_C}(\mathbf{r};t)+\mathbf{E_{TMS}}(\mathbf{r};t)\cdot\mathbf{J_C}(\mathbf{r};t)-\mathbf{E_C}(\mathbf{r};t)\cdot\mathbf{J_{TMS}}(\mathbf{r};t)\,d\mathbf{V}.\quad(\mathrm{S8})$$

Assuming sources $\mathbf{J_{TMS}}(\mathbf{r};t)$ and $\mathbf{J_C}(\mathbf{r};t)$ can be enclosed by a finite sized sphere, for an infinite radius sphere $\frac{\mathbf{H_C}(\mathbf{r};t)=\hat{\mathbf{r}}\times\mathbf{E_C}(\mathbf{r};t)}{\eta}$, $\mathbf{H_{TMS}}(\mathbf{r};t)=\hat{\mathbf{r}}\times\frac{\mathbf{E_{TMS}}(\mathbf{r};t)}{\eta}$ and $\mathbf{E_{TMS}}(\mathbf{r};t)\cdot\hat{\mathbf{r}}=\mathbf{H_{TMS}}(\mathbf{r};t)\cdot\hat{\mathbf{r}}=\mathbf{E_C}(\mathbf{r};t)\cdot\hat{\mathbf{r}}=\mathbf{H_C}(\mathbf{r};t)\cdot\hat{\mathbf{r}}=0$, where η is the impedance of free-space (Kong, 1986). Integrating Eq. (8) over all of space

$$\int_{\partial\mathbb{R}^3}\left(\mathbf{E_C}(\mathbf{r};t)\times\left(\hat{\mathbf{r}}\times\frac{\mathbf{E_{TMS}}(\mathbf{r};t)}{\eta}\right)-\mathbf{E_{TMS}}(\mathbf{r};t)\times\left(\hat{\mathbf{r}}\times\frac{\mathbf{E_C}(\mathbf{r};t)}{\eta}\right)\right)\cdot d\mathbf{r}=$$
$$\int_{\mathbb{R}^3}\mathbf{H_C}(\mathbf{r};t)\cdot\mathbf{K_{TMS}}(\mathbf{r};\mathrm{t})-\mathbf{H_{TMS}}(\mathbf{r};t)\cdot\mathbf{K_C}(\mathbf{r};\mathrm{t})+\mathbf{E_{TMS}}(\mathbf{r};\mathrm{t})\cdot\mathbf{J_C}(\mathbf{r};t)-\mathbf{E_C}(\mathbf{r};\mathrm{t})\cdot\mathbf{J_{TMS}}(\mathbf{r};t)\,d\mathbf{V}.\quad(\mathrm{S9})$$

The vector identity $\mathbf{A}\times(\mathbf{B}\times\mathbf{C})=\mathbf{B}(\mathbf{A}\cdot\mathbf{C})-\mathbf{C}(\mathbf{A}\cdot\mathbf{B})$ applied to the left hand side of Eq. (S9) results in $\hat{\mathbf{r}}\left(\mathbf{E_C}(\mathbf{r};t)\cdot\frac{\mathbf{E_{TMS}}(\mathbf{r};t)}{\eta}\right)-\frac{\mathbf{E_{TMS}}(\mathbf{r};t)}{\eta}(\mathbf{E_C}(\mathbf{r};t)\cdot\hat{\mathbf{r}})-\hat{\mathbf{r}}\left(\mathbf{E_{TMS}}(\mathbf{r};t)\cdot\frac{\mathbf{E_C}(\mathbf{r};t)}{\eta}\right)+\frac{\mathbf{E_C}(\mathbf{r};t)}{\eta}(\mathbf{E_{TMS}}(\mathbf{r};t)\cdot\hat{\mathbf{r}})=0$. The final form of reciprocity is

$$\int_{\mathbb{R}^3}\mathbf{H_C}(\mathbf{r};t)\cdot\mathbf{K_{TMS}}(\mathbf{r};t)-\mathbf{H_{TMS}}(\mathbf{r};t)\cdot\mathbf{K_C}(\mathbf{r};t)+\mathbf{E_{TMS}}(\mathbf{r};t)\cdot\mathbf{J_C}(\mathbf{r};t)-\mathbf{E_C}(\mathbf{r};t)\cdot\mathbf{J_{TMS}}(\mathbf{r};t)\,d\mathbf{V}=0.\,(\mathrm{S10})$$

Eq. (S10) is the general statement of reciprocity. Equation (3) follows from setting $\mathbf{K_{TMS}}(\mathbf{r};t)=\mathbf{K_C}(\mathbf{r};t)=0$ and Eq. (S21) follows from setting $\mathbf{K_C}(\mathbf{r};t)=\mathbf{J_{TMS}}(\mathbf{r};t)=0$. Here we assumed that $\sigma(\mathbf{r})$ was a scalar. These equations remain valid for symmetric tensor conductivities $\bar{\bar{\boldsymbol{\sigma}}}(\mathbf{r})$ because we only require that $\mathbf{E_C}(\mathbf{r};t)\cdot\bar{\bar{\boldsymbol{\sigma}}}(\mathbf{r})\mathbf{E}(\mathbf{r};t)=\mathbf{E}(\mathbf{r};t)\cdot\bar{\bar{\boldsymbol{\sigma}}}(\mathbf{r})\mathbf{E_C}(\mathbf{r};t)$. By same reasoning it is also valid for symmetric tensor permeabilities $\overline{\overline{\boldsymbol{\mu}_r}}(\mathbf{r})$ and permittivities $\overline{\overline{\boldsymbol{\epsilon}}}_r(\mathbf{r})$.

Derivation of E-field outside head for reciprocal scenario

Here we briefly derive the equations for the scenario that is reciprocal to TMS (i.e. MEG). A more detailed derivation is presented in (Ilmoniemi and Sarvas, 2019). We assume that impressed currents $\mathbf{J}_\mathbf{C}(\mathbf{r}) = p(t)\mathbf{J}_\mathbf{C}(\mathbf{r})$ inside the conductive head generate an E-field. The head is assumed to have conductivity distribution $\overline{\overline{\boldsymbol{\sigma}}}(\mathbf{r})$ and a magnetic permeability μ_0. At the low frequencies used for TMS quasi-stationary assumptions are valid, and the temporal variation and spatial variation are separable. Furthermore, we can neglect displacement currents to obtain the following quasi-static Maxwell's equations

$$\nabla \times \mathbf{E}_\mathbf{C}(\mathbf{r};t) = -\mu_0 \frac{d}{dt}\mathbf{H}_\mathbf{C}(\mathbf{r};t), \tag{S11}$$

$$\nabla \times \mathbf{H}_\mathbf{C}(\mathbf{r};t) = \mathbf{J}_\mathbf{C}(\mathbf{r};t) + \overline{\overline{\boldsymbol{\sigma}}}(\mathbf{r})\mathbf{E}_\mathbf{C}(\mathbf{r};t), \tag{S12}$$

and

$$\nabla \cdot \mu_0 \mathbf{H}_\mathbf{C}(\mathbf{r};t) = 0, \tag{S13}$$

Eq. (S13) implies that the magnetic flux $\mu_0\mathbf{H}_\mathbf{C}(\mathbf{r};t)$ is purely rotational, as such, it can be expressed in terms of a vector potential $\mu_0\mathbf{H}_\mathbf{C}(\mathbf{r};t) = \nabla \times \mathbf{A}_\mathbf{C}(\mathbf{r};t)$. Furthermore, we can assume any value for the divergence of $\mathbf{A}_\mathbf{C}(\mathbf{r};t)$. Here we choose $\nabla \cdot \mathbf{A}_\mathbf{C}(\mathbf{r};t) = 0$ (i.e. a Coulomb gauge). Rewriting Eq. (S12) in terms of $\mathbf{A}_\mathbf{C}(\mathbf{r};t)$

$$\begin{gathered}\nabla \times \nabla \times \mathbf{A}_\mathbf{C}(\mathbf{r};t) = \nabla\big(\nabla \cdot \mathbf{A}_\mathbf{C}(\mathbf{r};t)\big) - \nabla^2\mathbf{A}_\mathbf{C}(\mathbf{r};t) = \\ -\nabla^2\mathbf{A}_\mathbf{C}(\mathbf{r};t) = \mu_0(\mathbf{J}_\mathbf{C}(\mathbf{r};t) + \overline{\overline{\boldsymbol{\sigma}}}(\mathbf{r})\mathbf{E}_\mathbf{C}(\mathbf{r};t)).\end{gathered} \tag{S14}$$

The solution to Eq. (4) can be determined via a Green's function as

$$\mathbf{A}_\mathbf{C}(\mathbf{r};t) = \frac{\mu_0}{4\pi}\int_{\text{Head}} \frac{\mathbf{J}_\mathbf{C}(\mathbf{r}';t) + \overline{\overline{\boldsymbol{\sigma}}}(\mathbf{r}')\mathbf{E}_\mathbf{C}(\mathbf{r}';t)}{\|\mathbf{r}-\mathbf{r}'\|}\,\mathrm{d}\mathbf{r}'. \tag{S15}$$

Furthermore, Eq. (S11) implies that

$$\nabla \times \left(\mathbf{E_C}(\mathbf{r};t) + \frac{d}{dt}\mathbf{A_C}(\mathbf{r};t) \right) = 0. \tag{S16}$$

As such, the rotational part of the E-field is $-\frac{d}{dt}\mathbf{A_C}(\mathbf{r};t)$. We let the irrotational part of the E-field be described by negative the gradient of a scalar potential $\phi_C(\mathbf{r}';t)$ (i.e. $\mathbf{E_C}(\mathbf{r};t) = -\nabla\phi_C(\mathbf{r}';t) - \frac{d}{dt}\mathbf{A_C}(\mathbf{r};t)$). Then, taking the divergence of Eq. (S12) yields

$$\nabla \cdot \left(\overline{\overline{\boldsymbol{\sigma}}}(\mathbf{r}) \left(-\nabla\phi_C(\mathbf{r}';t) - \frac{d}{dt}\mathbf{A_C}(\mathbf{r};t) \right) + \mathbf{J_C}(\mathbf{r};t) \right) = 0. \tag{S17}$$

The quasi-stationary assumptions dictate that inside the head $\left\| \frac{d}{dt}\mathbf{A_C}(\mathbf{r};t) \right\| \ll \|\nabla\phi_C(\mathbf{r}';t)\|$ and we can neglect $\frac{d}{dt}\mathbf{A_C}(\mathbf{r};t)$. This results in $\mathbf{E_C}(\mathbf{r};t) = -\nabla\phi_C(\mathbf{r};t)$ and $-\nabla \cdot p(t)\mathbf{J_C}(\mathbf{r}) = -\nabla \cdot \overline{\overline{\boldsymbol{\sigma}}}(\mathbf{r})\nabla\phi_C(\mathbf{r};t)$ being true inside the head. The quasi-stationary assumptions further enable the separation of the temporal and spatial variation of the E-field. Hence, $\mathbf{E_C}(\mathbf{r};t) = p(t)\mathbf{E_C}(\mathbf{r}) = -p(t)\nabla\phi_C(\mathbf{r})$, where $-\nabla \cdot \mathbf{J_C}(\mathbf{r}) = -\nabla \cdot \overline{\overline{\boldsymbol{\sigma}}}(\mathbf{r})\nabla\phi_C(\mathbf{r})$. Outside the head, because we neglect displacement currents and there are no free charges, we have the opposite conditions, $\nabla\phi_C(\mathbf{r}';t) \approx 0$. As such,

$$\mathbf{E_C}(\mathbf{r};t) = p'(t)\mathbf{E_C}(\mathbf{r}) = -\frac{d}{dt}\mathbf{A_C}(\mathbf{r};t) = -p'(t)\frac{\mu_0}{4\pi}\int_{\text{Head}} \frac{\mathbf{J_C}(\mathbf{r}') + \overline{\overline{\boldsymbol{\sigma}}}(\mathbf{r}')\mathbf{E_C}(\mathbf{r}')}{\|\mathbf{r}-\mathbf{r}'\|}\,\mathrm{d}\mathbf{r}'. \tag{S18}$$

Reciprocity method applied to magnetic dipole coil models

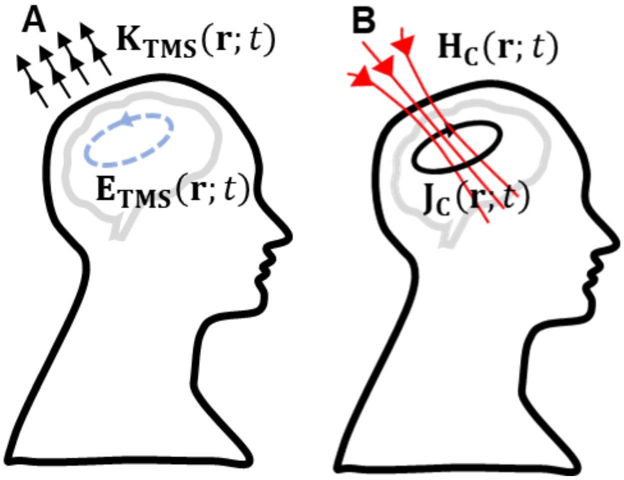

Figure S1. Alternative reciprocal scenarios: (A) Magnetic dipoles representing the TMS coil generate an E-field inside the cortex. (B) A brain current source generates a magnetic field (H-field) where the coil resides.

Presented here is an alternative reciprocity formulation that allows the use of a magnetic dipole model for the TMS coil. In this case, electromagnetic reciprocity is an equivalence relationship between two scenarios (Fig. S1). In one scenario, the TMS coil, modeled as impressed magnetic currents $\mathbf{K_{TMS}}(\mathbf{r};t) = p'(t)\mathbf{K_{TMS}}(\mathbf{r})$, generates an E-field $\mathbf{E_{TMS}}(\mathbf{r};t) = p'(t)\mathbf{E_{TMS}}(\mathbf{r})$ inside the head (Fig. S1A). In the second scenario, a source current $\mathbf{J_C}(\mathbf{r};t) = p(t)\mathbf{J_C}(\mathbf{r})$ inside the head generates an H-field $\mathbf{H_C}(\mathbf{r};t) = p(t)\mathbf{H_C}(\mathbf{r})$ where the coil resides (Fig. S1B). Reciprocity dictates that the reaction integral between $\mathbf{E_{TMS}}(\mathbf{r};t)$ and $\mathbf{J_C}(\mathbf{r};t)$ is equal to the reaction integral between $\mathbf{K_{TMS}}(\mathbf{r};t)$ and $\mathbf{H_C}(\mathbf{r};t)$,

$$\int \mathbf{E_{TMS}}(\mathbf{r};\mathrm{t}) \cdot \mathbf{J_C}(\mathbf{r};\mathrm{t})d\mathbf{r} = -\int \mathbf{H_C}(\mathbf{r};\mathrm{t}) \cdot \mathbf{K_{TMS}}(\mathbf{r};\mathrm{t})d\mathbf{r}\ . \tag{S19}$$

Here we choose $\mathbf{J_C}(\mathbf{r};t) = 0$ outside of the ROI and $\mathbf{J_C}(\mathbf{r};t) = p(t)V_{ROI}^{-1}\hat{\mathbf{t}}$ inside it. Reciprocity results in the following equation for the average E-field along $\hat{\mathbf{t}}$ in the ROI

$$\langle \mathbf{E_{TMS}}(\mathbf{r}) \cdot \hat{\mathbf{t}} \rangle = -\int \mathbf{H_C}(\mathbf{r}) \cdot \mathbf{K_{TMS}}(\mathbf{r})d\mathbf{r}\ . \tag{S20}$$

Note that the temporal variation has been factored out in this equation. In what follows, the temporal variation of all currents and E-fields is $p(t)$ and $p'(t)$, respectively, and is suppressed in the notation, as in the main text.

Computing $\langle \mathbf{E}_{\mathbf{TMS}}(\mathbf{r}) \cdot \hat{\mathbf{t}} \rangle$ using Eq. (S20) requires the evaluation of $\mathbf{H}_{\mathbf{C}}(\mathbf{r})$ outside the conductive head. This is done by computing the primary H-field due to the cortical current $\mathbf{J}_{\mathbf{C}}(\mathbf{r})$ and secondary H-field due to conduction currents $\overline{\overline{\boldsymbol{\sigma}}}(\mathbf{r})\mathbf{E}_{\mathbf{C}}(\mathbf{r})$, where $\overline{\overline{\boldsymbol{\sigma}}}(\mathbf{r})$ is the conductivity tensor inside the head,

$$\mathbf{H}_{\mathbf{C}}(\mathbf{r}) = \frac{1}{4\pi} \nabla \times \int_{\text{Head}} \frac{\mathbf{J}_{\mathbf{C}}(\mathbf{r}') + \overline{\overline{\boldsymbol{\sigma}}}(\mathbf{r}')\mathbf{E}_{\mathbf{C}}(\mathbf{r}')}{\|\mathbf{r} - \mathbf{r}'\|} \mathrm{d}\mathbf{r}' \quad . \tag{S21}$$

Finally, to estimate Eqs. (S20)–(S21) we use the same approach as described in the main text to estimate Eqs. (2)–(3). Specifically, Eqs. (5)–(6) become, respectively,

$$\mathbf{H}_{\mathbf{C}}(\mathbf{r}) = -\frac{1}{4\pi} \sum_{j=1}^{N} \mathbf{I}_{\mathbf{C}}^{(j)} \times \nabla \frac{1}{\left\| \mathbf{r} - \mathbf{r}_{\mathbf{C}}^{(j)} \right\|} \ . \tag{S22}$$

and

$$\langle \mathbf{E}(\mathbf{r}) \cdot \hat{\mathbf{t}} \rangle = \frac{1}{4\pi} \sum_{i=1}^{M} \mathbf{K}_{\mathbf{coil}}^{(i)} \cdot \sum_{j=1}^{N} \mathbf{I}_{\mathbf{C}}^{(j)} \times \nabla \frac{1}{\left\| \mathbf{r}_{\mathbf{coil}}^{(i)} - \mathbf{r}_{\mathbf{C}}^{(j)} \right\|} \ , \tag{S23}$$

where magnetic dipoles $\mathbf{K}_{\mathbf{coil}}^{(i)}$ at locations $\mathbf{r}_{\mathbf{coil}}^{(i)}$ model the coil and $i = 1,2, \ldots, M$.

Validation comparison between simulations with SimNIBS and in-house FEM solver

Here additional validation results are given indicating that our in-house FEM implementation (Gomez et al., 2020) produces E-field simulation results and error levels comparable to those of SimNIBS, a commonly used non-invasive brain stimulation simulation package (Saturnino et al., 2019; SimNIBS Developers, 2020; Thielscher et al., 2015). Fig. S2 shows spherical head model results indicating that the SimNIBS errors are slightly higher than our direct FEM (see Fig. 3 in the main text). These small differences in accuracy are likely due to differences in the way that the primary E-field is computed. Fig. S3 compares the results obtained for the Ernie head model via our direct FEM with SimNIBS, indicating a maximum relative difference across all simulations of 0.11%. Fig. S4 compares results obtained for the four additional models (M1–M4) obtained via our direct FEM and SimNIBS. The agreement between the two sets of solutions increases with ROI size. This is likely because we compute the average the E-field on the ROI, which is less sensitive to numerical errors with increasing ROI size. In all cases, SimNIBS was in agreement with our direct FEM to a fraction of a percentage indicating that both implementations practically provide the same solution.

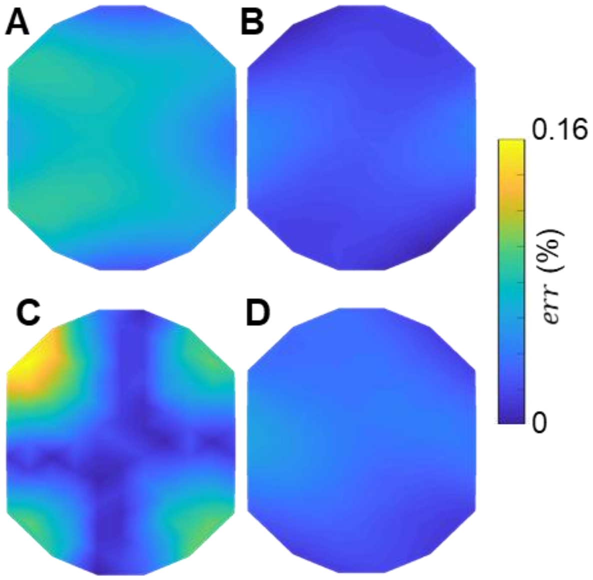

Figure S2. Error in SimNIBS E-field simulations relative to analytical solution in sphere head model, analogous to Fig. 3 in the main text. The plots show err observed at each scalp location for coil orientations of (A) 0°, (B) 45°, (C) 90°, and (D) 135°.

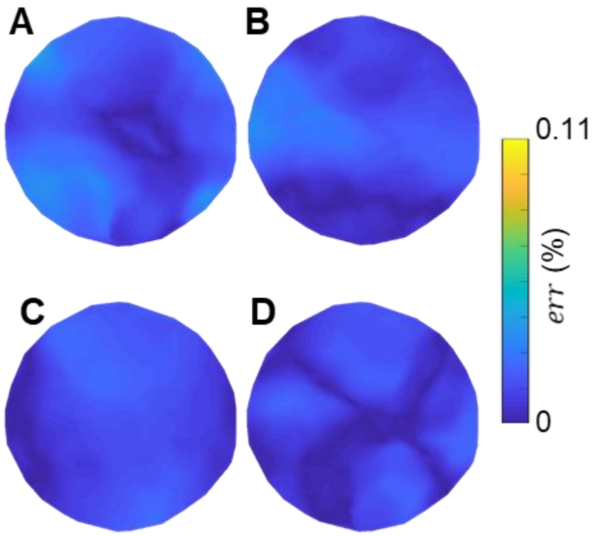

Figure S3. Difference in SimNIBS simulation results for Ernie head model relative to our direct FEM results, analogous to Fig. 4 in the main text. The plots show err observed at each scalp location for coil orientations of (A) 0°, (B) 45°, (C) 90°, and (D) 135°.

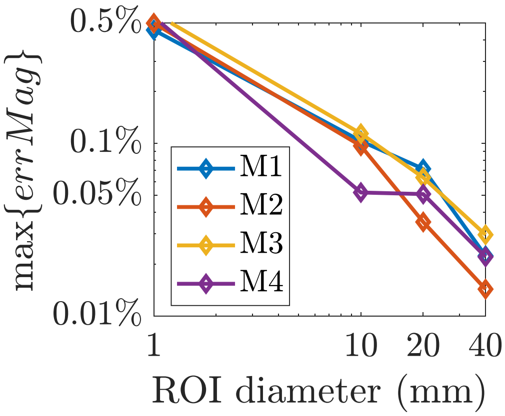

Figure S4. Maximum normalized relative difference for the average E-field magnitude in the SimNIBS 3.1 simulations compared to our direct FEM results for head models M1–M4.

Additional coil placement optimization results

Fig. S5 shows coil placement optimization results analogous to Fig. 9E–T in the main text but comparing ADM with our in-house direct FEM solver instead of SimNIBS. As in the main results, the optimized placements for the two methods match closely, especially for small ROI sizes.

Tables S1 and S2 provide further quantitative comparisons of ADM, the SimNIBS direct optimization method, and conventional ROI center of mass (CM) placement. In Table S1, we observe that the optimized coil placements deliver improved E-field relative to the coil placement above the ROI CM. Furthermore, the optimized coil orientation and the orientation normal to the sulcal wall can differ by as much as 62°. In Tables S2 we additionally compare $\|\langle \mathbf{E}_{\mathbf{ADM}}(\mathbf{r})\rangle\|$ and $\langle\|\mathbf{E}_{\mathbf{SimN}}(\mathbf{r})\|\rangle$ for ROIs of varying sizes. For ROIs with diameter of 20 mm or less the relative difference of the maximum E-field magnitude is less than 0.7%, which is below the numerical errors of the FEM solver (Gomez et al., 2020).

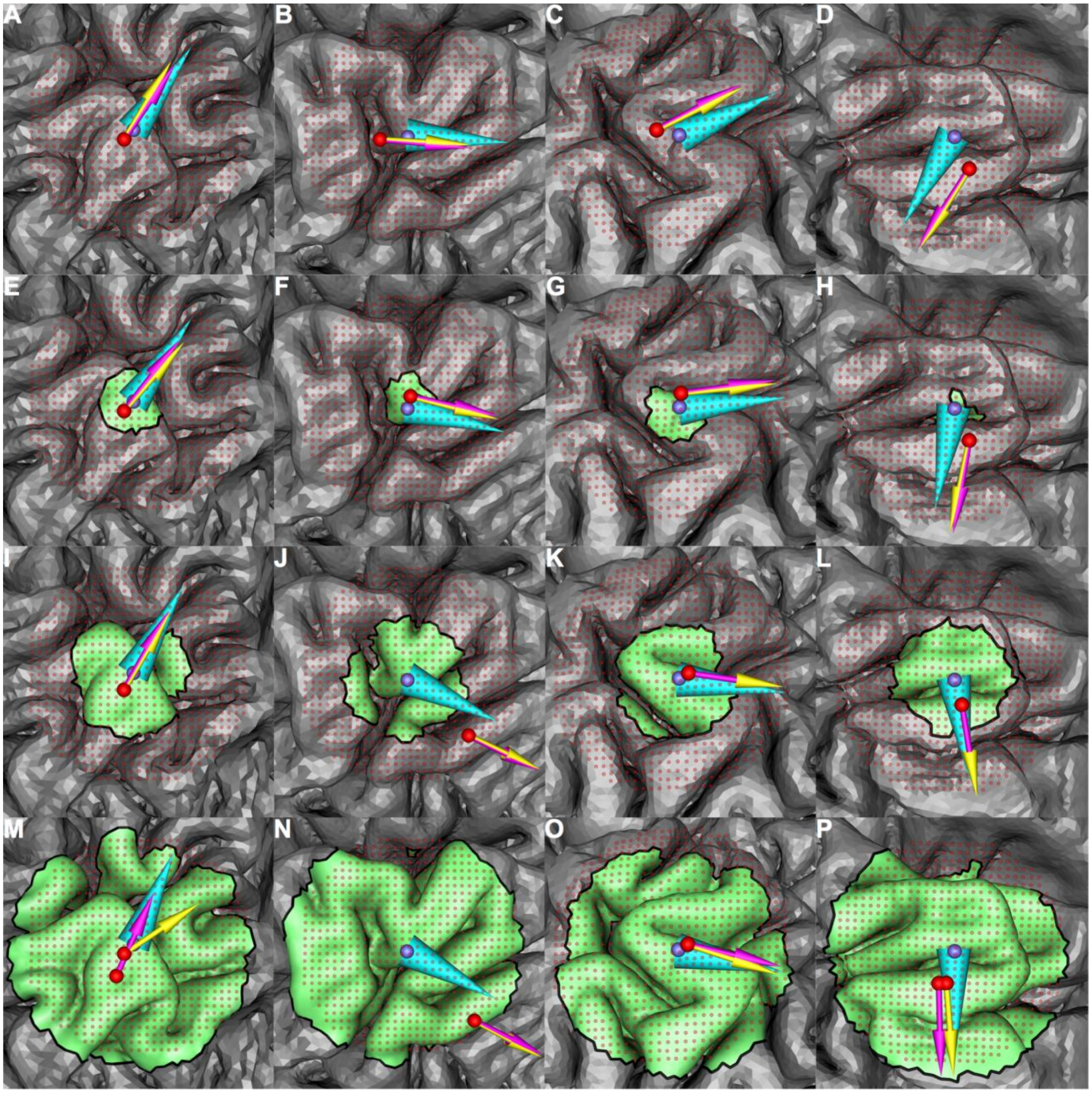

Figure S5. Coil placement results for models M1–M4 (left to right columns) for ROIs of increasing size (top to bottom rows). The in-house direct FEM optimized and ADM optimized position and orientation are represented by the pink and yellow arrow, respectively, $\hat{\mathbf{t}}_{\mathbf{opt}}$ and the ROI CM are represented by cyan cone and purple sphere, respectively. The rows show, top to bottom, the results for ROI diameter of 1 (1 tetrahedron), 10, 20, and 40 mm. In most cases both optimization methods result in the same or similar coil position and orientation.

Model	ROI diameter [mm]	$\lVert\mathbf{R}_{\mathbf{CM}} - \mathbf{R}_{\mathbf{SimN}}\rVert$ [mm]	$\lvert\theta_{CM} - \theta_{SimN}\rvert$ [°]	$\left(\frac{\langle\lVert\mathbf{E}_{\mathbf{CM}}(\mathbf{r})\rVert\rangle}{\langle\lVert\mathbf{E}_{\mathbf{SimN}}(\mathbf{r})\rVert\rangle} - \mathbf{1}\right)$ [%]	$\lVert\mathbf{R}_{\mathbf{CM}} - \mathbf{R}_{\mathbf{ADM}}\rVert$ [mm]	$\lvert\theta_{CM} - \theta_{ADM}\rvert$ [°]	$\left(\frac{\lVert\langle\mathbf{E}_{\mathbf{CM}}(\mathbf{r})\rangle\rVert}{\lVert\langle\mathbf{E}_{\mathbf{ADM}}(\mathbf{r})\rangle\rVert} - \mathbf{1}\right)$ [%]
M1	1	1.86	35.7	-3.04	1.86	37.7	-2.89
	10	1.86	35.7	-1.58	1.86	33.7	-1.53
	20	2.67	41.1	-1.87	2.67	42.1	-1.62
	40	1.86	16.0	-0.26	4.94	47.5	1.83
M2	1	3.90	62.0	-5.75	3.90	60.0	-5.75
	10	1.95	51.0	-4.71	1.95	53.0	-4.80
	20	11.57	42.0	-4.88	11.57	41.0	-4.62
	40	13.79	39.0	-5.73	13.79	41.0	-3.46
M3	1	1.61	18.1	-0.91	2.97	10.7	-0.63
	10	1.61	33.1	-1.66	1.61	31.1	-1.30
	20	1.34	47.3	-3.67	1.34	47.3	-3.15
	40	1.34	57.3	-3.93	1.34	52.3	-2.81
M4	1	4.29	5.92	-1.08	4.29	3.97	-1.30
	10	4.29	20.9	-1.67	4.29	22.9	-1.38
	20	3.06	41.7	-3.02	3.06	41.7	-2.39
	40	4.05	36.9	-3.41	4.48	33.8	-1.52

Table S1. Comparisons between placing the coil above the ROI center of mass (CM) versus where it maximizes the ROI average E-field magnitude with the SimNIBS 3.1 direct or ADM methods. Note that the average E-field magnitude is computed differently for the two optimization methods: $\langle\lVert\cdot\rVert\rangle$ for SimNIBS comparisons and $\lVert\langle\cdot\rangle\rVert$ for ADM comparisons.

Model	ROI diameter [mm]	$\lVert\mathbf{R}_{\mathbf{ADM}} - \mathbf{R}_{\mathbf{SimN}}\rVert$ [mm]	$\lvert\theta_{ADM} - \theta_{SimN}\rvert$ [°]	$\left(\frac{\lVert\langle\mathbf{E}_{\mathbf{ADM}}(\mathbf{r})\rangle\rVert}{\langle\lVert\mathbf{E}_{\mathbf{SimN}}(\mathbf{r})\rVert\rangle} - \mathbf{1}\right)$ [%]
M1	1	0.00	2	-0.15
	10	0.00	2	-0.049
	20	0.00	1	-0.25
	40	3.20	32	-2.1
M2	1	0.00	2	-0.0035
	10	0.00	2	0.095
	20	0.00	1	-0.28
	40	0.00	2	-2.4
M3	1	3.33	7.6	-0.28
	10	0.00	2	-0.36
	20	0.00	0	-0.54
	40	0.00	5	-1.2
M4	1	0.00	4	0.23
	10	0.00	2	-0.3
	20	0.00	0	-0.65
	40	1.00	3.25	-1.9

Table S2. Comparisons between using the SimNIBS 3.1 direct method to maximize the E-field magnitude (i.e. maximize $\langle\lVert\cdot\rVert\rangle$) and using ADM to approximately maximize the E-field magnitude (i.e. maximize $\lVert\langle\cdot\rangle\rVert$). Unlike in the main text and Table S1, we compare the methods using their respective ROI E-field metrics to emphasize that the E-field magnitude approximation $\lVert\langle\cdot\rangle\rVert$ gives a good estimate of the actual average E-field magnitude.

Fig. S6 explores the difference in E-field distribution for coil placement over the ROI CM and ADM optimal coil placement for relatively large ROIs (20 mm and 40 mm diameter). Compared to the ADM results, the E-field for CM placement is more equally distributed within the ROIs. However, the ADM results show peak E-field increased by 6.03% and 8.55%, respectively, which is sufficient to raise the averaged E-field of the ROI by 2.0% and 2.6%, respectively, compared to the coil position over the ROI CM. These results illustrate that the optimal coil placement is significantly influenced by the individual head anatomy, including the coil-to-cortex distance, which was over 8 mm smaller for the optimal coil position than over the CM for both ROIs.

Fig. S7 evaluates ADM implemented in SimNIBS 3.2 compared to its direct optimization method, showing similar results in optimizing E-field magnitude and identical results for directional E-field objectives for various types of ROIs: auditory cortex ROI spanning portions of the crown and wall around the gyrus lip (first column), visual cortex ROI on a gyral crown (second column), and motor cortex ROI distributed across two hemispheres corresponding approximately to toe representation in homunculus (third column). Since the TMS induced E-field is predominantly tangential to the scalp, for the ROI on top of the gyri in the visual cortex (Fig. S7K), we used a directional E-field objective utilizing $\hat{\mathrm{t}}$ derived from the cross product between $\hat{\mathrm{t}}_{\mathrm{opt}}$ (see Fig. S7H) with the mostly scalp-radial normal to the cortical surface—this choice is of direction is rather arbitrary as there is no intrinsic preferred E-field direction for ROIs center of a gyral crown. In these examples, the search space for the optimal coil placement was restricted to 10 mm radius around the ROI CM with 1 mm grid spacing on the scalp and the coil orientation was discretized in 10° steps. The SimNIBS 3.2 direct optimization method required about 6.5 hours of overall runtime, whereas ADM completed the optimization in 6 minutes.

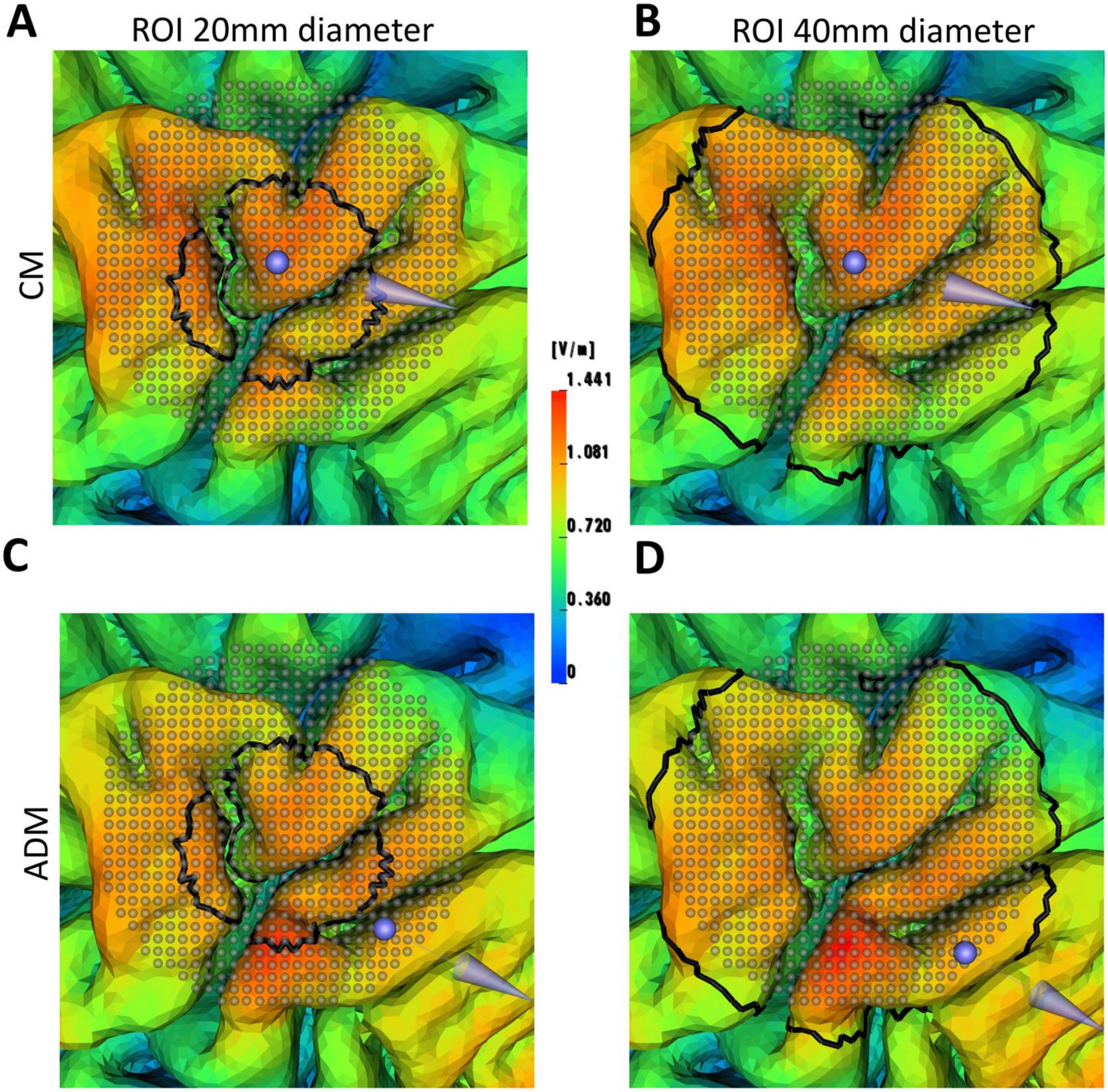

Figure S6. Examples of E-field magnitude map for optimal coil placement located over 1 cm away from ROI CM placement. Results were generated with SimNIBS 3.2 for Model M2 with ROI diameters of 20 and 40 mm, reproducing setup in Fig. 9N,R and Fig. S5J,N. (A,B): Coil positioned at scalp-projected ROI CM and oriented to maximize ROI E-field. (C,D): Coil placement optimized with ADM. All coil candidate locations are depicted as transparent gray spheres, whereas the chosen coil placement to compute the E-field is indicated with purple sphere and arrow. Heat map indicates E-field magnitude for coil current with dI/dt = 1 A/µs.

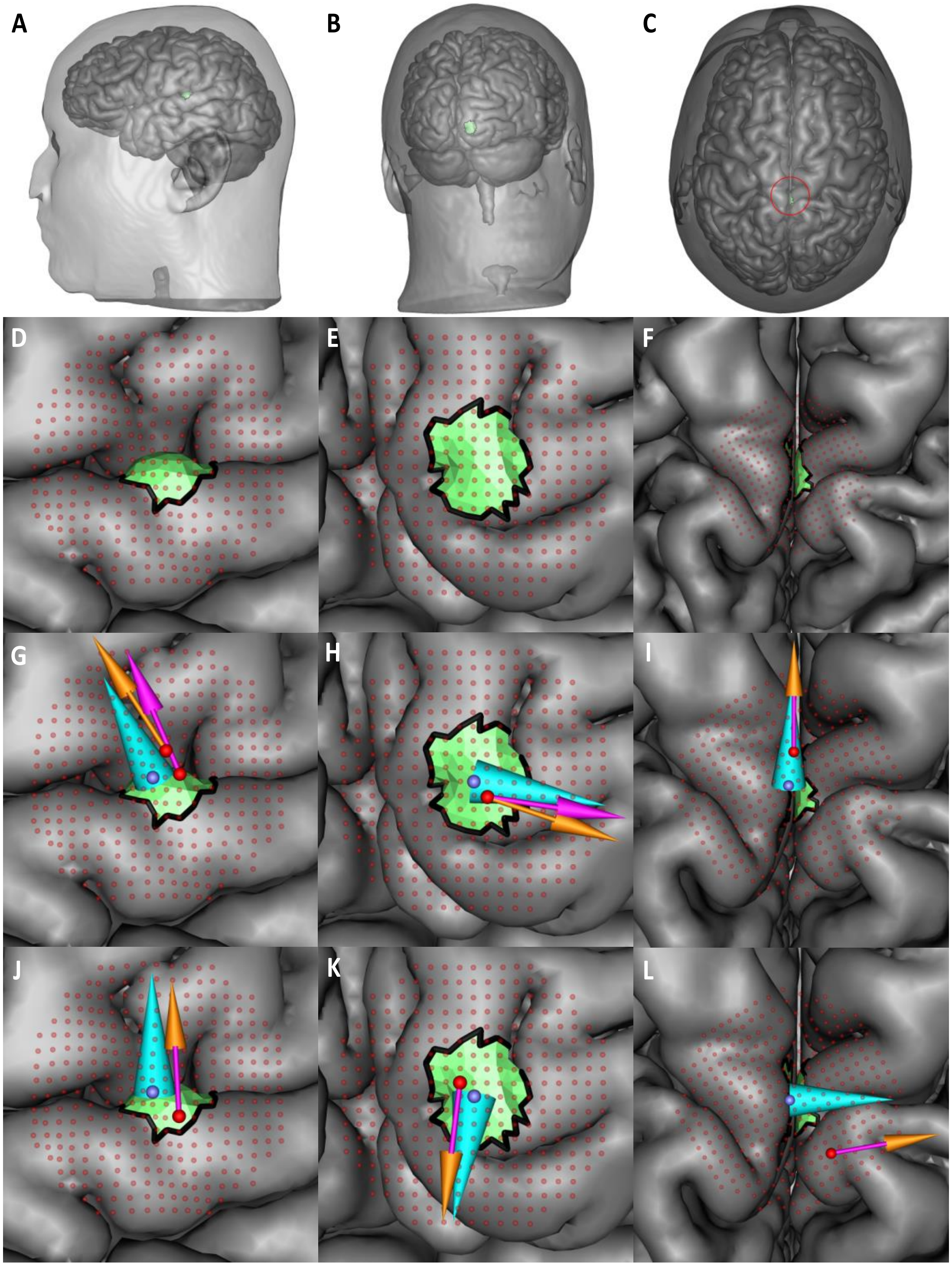

Figure S7. Comparison of computational TMS coil placement optimization for three anatomical ROIs of 5 mm radius in Ernie head model. Compared are direct method (pink arrow) and ADM (orange arrow), both implemented in SimNIBS 3.2, as well as scalp projection of ROI CM (purple sphere). ROIs include: primary auditory cortex, partially in sulcal wall (A,D); primary visual cortex, on gyral crown (B,E), and motor cortex around interhemispheric fissure, distributed across both hemispheres (C,F). G–I: Coil placement for maximizing average ROI E-field magnitude; cyan cone represents $\hat{\mathbf{t}}_{\mathbf{opt}}$. J–L: Coil placement to maximize average ROI E-field component along selected direction $\hat{\mathbf{t}}$ represented by cyan cone.

References

Balanis, C.A., 1999. Advanced engineering electromagnetics. John Wiley & Sons.

Gomez, L.J., Dannhauer, M., Koponen, L.M., Peterchev, A.V., 2020. Conditions for numerically accurate TMS electric field simulation. Brain Stimul 13, 157-166.

Harrington, R., 2001. Time-harmonic electromagnetic fields/Harrington RF–New-York, Chichester. Weinheim, Brisbane, Singapore, Toronto: John Wiloy&Sons. Inc.

Ilmoniemi, R.J., Sarvas, J., 2019. Brain Signals: Physics and Mathematics of MEG and EEG. MIT Press.

Kong, J., 1986. Electromagnetic Wave Theory,. JohnWiley & Sons. New York.

Plonsey, R., 1972. Capability and limitations of electrocardiography and magnetocardiography. IEEE Transactions on Biomedical Engineering, 239-244.

Saturnino, G.B., Madsen, K.H., Thielscher, A., 2019. Electric field simulations for transcranial brain stimulation using FEM: an efficient implementation and error analysis. J Neural Eng 16, 066032.

SimNIBS Developers, 2020. SimNIBS. https://simnibs.github.io/simnibs.

Thielscher, A., Antunes, A., Saturnino, G.B., 2015. Field modeling for transcranial magnetic stimulation: A useful tool to understand the physiological effects of TMS? , 2015 37th Annual International Conference of the IEEE Engineering in Medicine and Biology Society (EMBC), pp. 222-225.